




Curved InGaAs nanowire array lasers grown directly on silicon-on-insulator

BOGDAN-PETRIN RATIU,¹  BALTHAZAR TEMU,¹ CRISTIAN MESSINA,¹ OUMAIMA ABOUZAIID,¹ SAMIR RIHANI,² GRAHAM BERRY,² SANG SOON OH,¹ AND QIANG LI^{1,*}

¹School of Physics and Astronomy, Cardiff University, CF24 3AA, United Kingdom

²Huawei Technologies Research and Development, Ipswich Research Centre, Ipswich, UK

*LiQ44@cardiff.ac.uk

Abstract: Catalyst-free, selective nano-epitaxy of III-V nanowires provides an excellent materials platform for designing and fabricating ultra-compact, bottom-up photonic crystal lasers. In this work, we propose a new type of photonic crystal laser with a curved cavity formed by InGaAs nanowires grown directly on silicon-on-insulator. This paper investigates the effect of the radius of the curved cavity on the emission wavelength, quality factor as well as laser beam emission angle. We find that the introduction of curvature does not degrade the quality factor of the cavity, thereby offering another degree of freedom when designing low-footprint multiwavelength photonic crystal nanowire lasers. The experimentally demonstrated device shows a lasing threshold of $157 \mu\text{J}/\text{cm}^2$ at room temperature at telecom O-band wavelengths.

Published by Optica Publishing Group under the terms of the [Creative Commons Attribution 4.0 License](https://creativecommons.org/licenses/by/4.0/). Further distribution of this work must maintain attribution to the author(s) and the published article's title, journal citation, and DOI.

1. Introduction

III-V photonic crystal (PhC) lasers have been widely studied due to their very high quality factors (Q factors) and low thresholds [1–6]. The ultra-low energy consumption and small device footprint make them highly attractive for Si based on-chip optical interconnects where achieving low energies per bit is of paramount importance [7]. Current high-performance air-hole based PhC lasers require wafer bonding or layer transfer process to be integrated onto a Si chip [8–11]. Epitaxial growth of III-V PhC laser cavities directly on Si is desirable for large scale monolithic integration with improved scalability, reliability, and reduced cost. However, this is prohibited by the material dissimilarities including lattice mismatch between III-V semiconductors and Si which give rise to high densities of threading dislocations diminishing device lifetimes [12]. Recently, optically pumped PhC lasers directly grown on CMOS-compatible Si substrate were demonstrated using conventional thin film heteroepitaxy [13]. However, a-few-micron thick buffer layers are needed to reduce the threading dislocation density and it is still challenging to couple light into Si waveguides. An attractive solution to bypass the constraints from lattice mismatch is growing nanowires. Epitaxial nanowire growth significantly reduces the contact area between the III-V nanowires and Si substrate and thus provides an efficient way to avoid the formation of threading dislocations by relaxing elastic strain towards the nanowire sidewalls [14,15]. Catalyst-free, selective area metal-organic chemical vapor deposition (MOCVD) allows the arrangement of nanowires into arbitrary shapes. This has previously been exploited to create 2D PhC band edge cavities and 1D PhC nanobeam cavities [16–20]. This technique can realize optically pumped lasers with low threshold at room temperature [17,18]. Light coupling from nanowire PhC array to Si passive waveguides was also achieved, demonstrating the potential of using nanowires as building blocks for on-chip optical links [17]. Due to the high Q factor, tunable resonance wavelength and slow-light effect of photonic crystals, other possible applications include spectrometry, photodetection, biosensing.

Previously, curved cavity PhCs such as micro-disk lasers and PhC micro-ring lasers have been proposed and demonstrated using top-down fabricated air-holes PhC structures [21–25]. This type of curved circular structures takes advantage of high Q factor whispering gallery modes and gain enhancing PhC slow light effects to achieve high efficiency devices, such as lasers, modulators, filters and sensors. However, due to the geometry and material mismatch of these devices, it can be difficult to monolithically integrate gain material into a SiPh circuit. Such designs have not been realized in the bottom-up nanowire platform yet. Here, we demonstrate a novel type of curved nanowire array laser by arranging nanowires into a circular arc geometry using site-controlled selective area nano-epitaxy [26]. The vertical and atomically flat nanowire sidewall surfaces, and the ability to form in-situ passivation layers in nanowire growth makes them less susceptible to propagation losses induced by waveguide sidewall roughness encountered in top-down fabricated devices [27]. Finite-difference time-domain (FDTD) simulations were carried out to study the resonant modes, Q factors, and emission direction of our devices. Curved nanowire arrays with varied radius and cavity length were fabricated. Under room-temperature pulsed excitation, we demonstrate multiwavelength lasing from 1290 to 1330 nm.

2. Methods

The nanowires were grown on a SOI substrate with a 52 nm (111) Si top layer and a 2- μm thick buried oxide layer. A 20 nm SiN layer was deposited and patterned using electron beam lithography and etched to expose the (111) Si surface underneath in small circular nanoholes of 30 nm in diameter. Prior to nanowire growth, the sample was dipped in a dilute 2.5% HF solution for 10 min to remove the native silicon oxide. The growth was carried out in an Aixtron Close Coupled Showerhead MOCVD reactor. The precursors used were triethylgallium (TEGa), trimethylindium (TMIn), tertiarybutyl arsine (TBAs) and tertiarybutyl phosphine (TBP). Hydrogen was used as the carrier gas with a reactor pressure of 50 mbar. A thermal desorption step was done at 850 °C for 20 min under hydrogen flow to remove any remaining traces of native oxide. The temperature was then lowered to 670 °C and a GaAs seeding layer was grown with a V/III ratio of 80. The InGaAs core layer was grown at a lower temperature of 610 °C to facilitate indium incorporation. Finally, a 15 nm InGaP shell layer was grown at a temperature of 570 °C for surface passivation. The resulting structure can be seen in Fig. 1 (a).

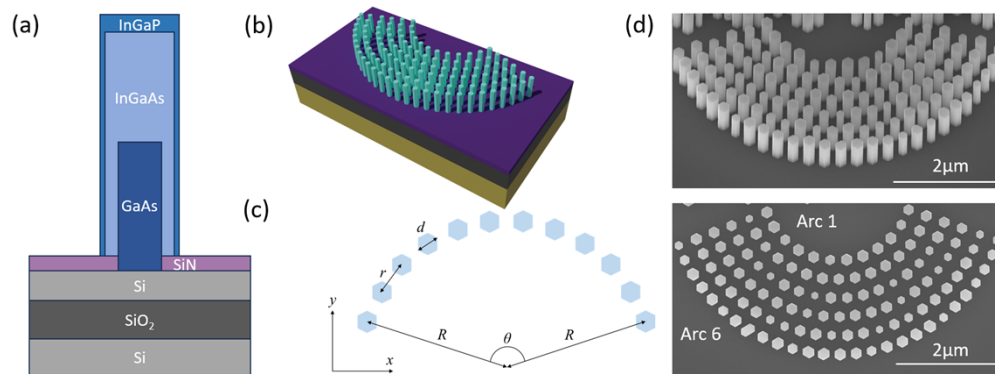


Fig. 1. (a) Cross section diagram of a single nanowire, (b) Schematic of the curved nanobeam arrays. (c) The relevant dimensions of a single nanowire arc. (d) SEM images of the curved array nanowire device.

As shown in Fig. 1 (b), the curved nanowire array consists of six circular arcs with a central angle θ of 140° and increasing radius R and pitch size r . The relevant dimensions of the curved nanobeam arcs are defined in Fig. 1 (c). The height of the nanowires is around 730 nm and the

diameter d is 220 nm, as measured from SEM images in Fig. 1 (d). Nanowire height is reasonably uniform, however the diameter exhibits non-uniformity with a distribution width of 11%. The arcs are positioned very close together to showcase the potential of using nanowire photonic crystals for high-density integration of multiwavelength telecom lasers.

3. Simulation results

To study the resonant properties of curved nanowire cavities, 3D FDTD simulations were performed using the Ansys Lumerical software. The nanowire array was meshed using a conformal mesh method with a minimum accuracy of 18 mesh points per wavelength. This is sufficient resolution, as increasing the mesh accuracy further does not change the results. The simulation region boundaries used PML boundary conditions on all sides, which were placed far enough away from the structure to not couple to the resonant cavity. To calculate the Q factors, we used the slope of the envelope of the decaying signal, computed using the high-Q monitor provided by Lumerical FDTD.

First, we simulated the full nanowire array structure corresponding to our fabricated structure (Fig. 1). Figure 2(a) shows the electric field profile of resonant modes taken at the plane half the height of the nanowires, indicating increasing resonant wavelength from arc 2 (1295 nm) to arc 6 (1340 nm). Here, the increase of resonant wavelength is due to the increase of both the spacing between nanowires and the cavity size defined by their arc length.

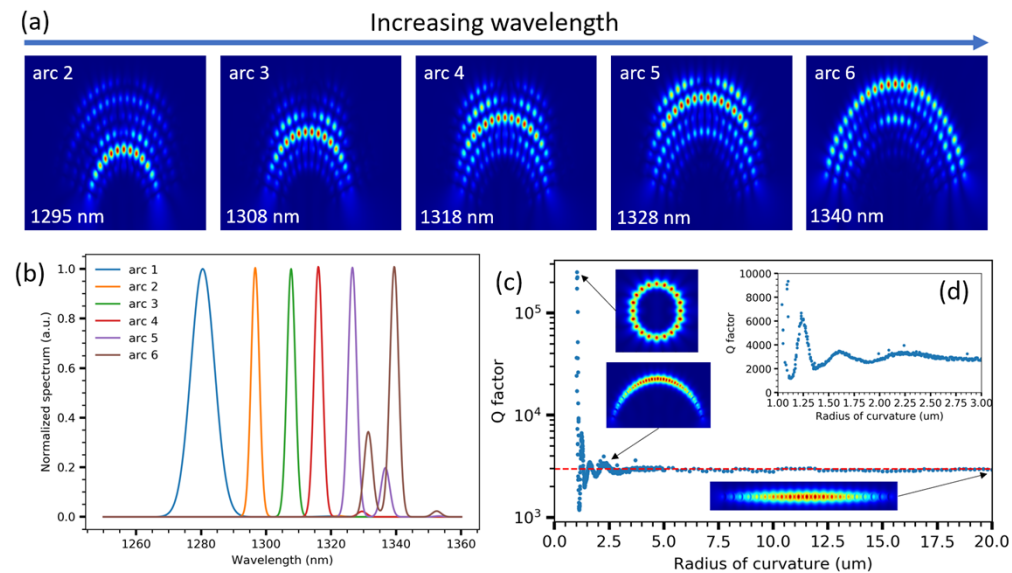


Fig. 2. FDTD simulation results showing (a) the electric field magnitude taken at a cross section through the middle of the nanowires at the resonant frequencies, (b) the normalized resonances of each individual nanowire arc, (c) the relationship between Q factor and the radius of curvature of an arc along with representative E-field mode profiles and a dashed line indicating the Q factor value of a straight nanobeam, and (d) an inset showing Q factor oscillations in greater detail.

To understand the origin of the resonances, additional 3D FDTD simulations were carried out for each individual arc separately and the simulated spectra are shown in Fig. 2(b). Interestingly, the resonant wavelengths from arc 1 to arc 6 shows excellent agreement with the resonance frequencies of the full array structure in Fig. 2(a). This suggests that the interactions between resonant modes in arcs are very small and the radiation from non-active arcs can be negligible

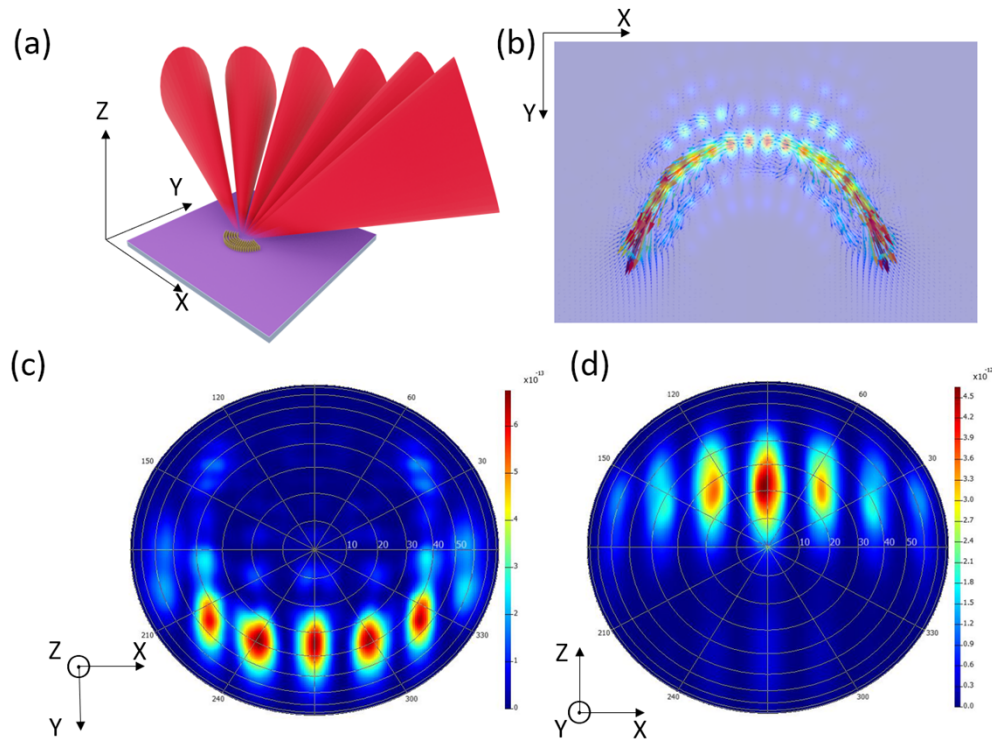


Fig. 3. Far field emission simulations of the full structure at a representative wavelength of 1318 nm. (a) diagram showing the free space emission of the structure, (b) Poynting vector map overlaid over the $|E|$ field showing the emission direction, (c) polar plot of the far field emission in the vertical (+z) direction and (d) polar plot of the far field emission in-plane (+y).

when one of the modes is lasing. This can be understood from the weak electric field profiles in non-active arcs in Fig. 2(a). Note that arc 1 could not form a visible resonant mode in the full array structure because it has very low Q factor, as manifested by the broad peak, due to its short cavity length. While arcs 2, 3 and 4 show single mode resonances, arcs 5 and 6 show multimode resonances due to their larger arc length.

Next, we look at the effect of the radius of curvature on the Q factor by simulating a single curved array with different radius of curvature values. We keep all other parameters the same including nanowire number, nanowire dimension, spacing and cavity length. Note that for the data set shown in Fig. 2(c), all simulations were done in two dimensions due to computational constraints. Although this 2D FDTD simulation setup eliminates the vertical loss both into the substrate and the air leading to a constant increase in the Q factor for all radius values, the couplings between the nanowires are well described. As one can expect, the curvature of the array has negligible impact on the lateral losses at large bending radii resulting in the Q factor very close to that of a straight array. Interestingly, in the opposite limit when value of bending radius is very small, the Q factor increases significantly due to the coupling between the fields at both ends of the array. The curved array eventually bends into a full circle which acts similarly to a micro-ring leading to very large Q factors. The oscillating behavior at small bending radius around 1-3 μm , shown in Fig. 2(d), can be correlated to distance between the two ends of the array. The coherent laser light exits the structure through the ends of the arrays, as shown in Fig. 3 (b). At smaller values of radius of curvature, the two ends will be close enough to each

other to be coupled together. Light exiting one end of the array can then be absorbed by the other end and recycled. As the emitted light is coherent, the distance between the two ends determines whether the absorbing end lies at a node or antinode of the emitted wave. If the absorbing end is placed at an antinode, the coupling strength between the ends of the array will be higher. If the absorbing end is placed at a node, the coupling strength will be lower. As the distance between the ends changes due to the change in radius in curvature, the ends go through peaks and troughs, causing the coupling, and thus the Q factor to oscillate.

A complete nanowire microring circle has been simulated to have a Q factor on the order of 10^5 . This resistance to bending losses showcases the ability of nanowire arrays to be bent into shapes similar to their hole-based PhC counterparts for applications such as microring lasers [21–25]. Although the Q factors for curved arrays are low compared to a full circle, they could be greatly improved by including nanowire-based reflectors at the two ends of the beam, tailoring the spacing between nanowires or decreasing the thickness of Si layer [16–18].

To predict the emission profile of the nanowire array lasers, the free space far field pattern of the resonant modes was calculated using the 3D FDTD method. First, we can expect the most of light is emitted from the ends of the nanowire arrays in the lateral direction (XY plane in Fig. 3(a)) similar to straight nanobeam lasers [17,18]. This can be seen from the Poynting vector plot in Fig. 3(b) which shows the power flux of the electromagnetic field is strongest at the ends of the array. The Poynting vector points tangentially away from the array showing the light is emitted towards the back of the array, in the + Y direction. There is no field flow towards the front of the array in the -Y direction, indicating that bending losses are negligible for this radius of curvature.

Because of the small cavity size, the two output beams have relatively large divergence. In the far field, the emission from the two ends will overlap and interfere. This is shown in Fig. 3(c) and (d), where multiple lobes can be seen. Figure 3(c) shows the far field emission as seen from the top of the array, confirming the preferentially directional emission towards the back of the array. The in-plane emission is shown in Fig. 3(d) where the same interference pattern can be seen again. The interference pattern azimuthal divergence angle is approximately 100° and the polar divergence angle is approximately 20° . Since the two ends of the array are not parallel to each other, the azimuthal divergence is large. This can be improved by aligning the ends of the array to point in the same direction, ensuring the emitted beams propagate parallel to each other. The radius of curvature was found to have a small impact on the polar divergence angle, giving a tuneability range of between 10° - 30° .

4. Experimental results

The optical properties of the curved nanowire array structure have been experimentally measured using room temperature micro-photoluminescence. Optical excitation was provided by a pulsed laser (YSL SC-PRO 7 supercontinuum source and AOTF-Pro tunable wavelength filter) with a 100 ps pulse width with a 1 MHz repetition rate at a wavelength of 633 nm. The laser beam was focused on a 6 μm diameter spot normally incident to the sample using a 50 \times infinity corrected objective lens (50X Mitutoyo Plan Apo NIR). The infrared light emitted by the sample was collected through the same lens and measured using an Acton SpectraPro SP-2750 spectrometer and a NIRvana 640 InGaAs focal plane array detector. A diagram of the micro-PL setup is shown in Fig. 4.

To verify the modes we observed match the simulated resonant modes shown in Fig. 2 (a), we selectively pump the array and measure the lasing threshold. A lower threshold signifies a higher overlap between the pumping spot and the resonant mode. The results are shown in Fig. 5 (a). When pumping on the side of the array the threshold is significantly higher, implying that the resonant mode is confined mainly to the center of the array, as expected from the simulation.

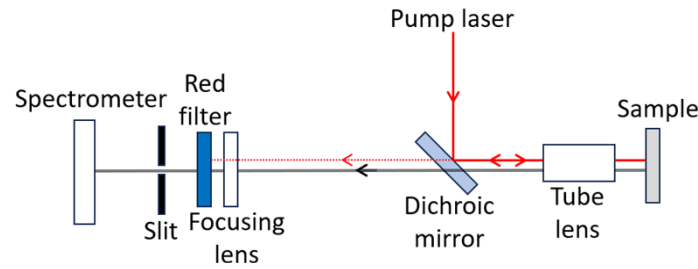


Fig. 4. Micro-PL experimental setup. The black line represents infrared emission from the sample. The dotted red line shows the residual pumping laser light that passes through the dichroic mirror.

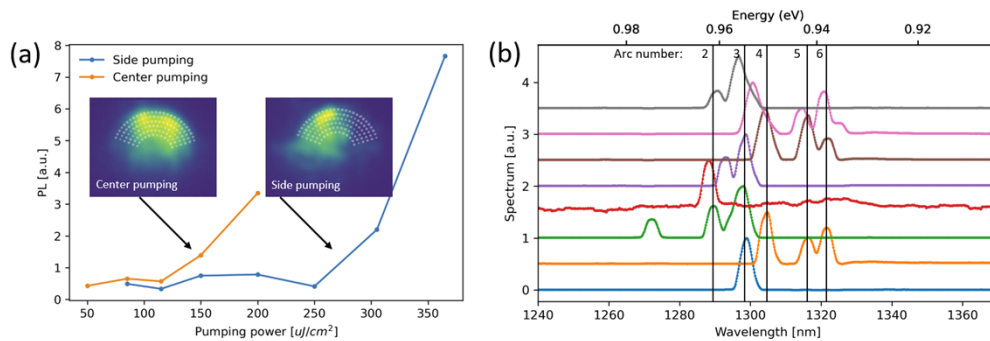


Fig. 5. (a) LL curves of the array pumped selectively in the center and on the side of the cavity, along with images showing the two pumping positions. (b) Lasing spectra of a few nominally identical nanowire arrays showing common lasing wavelengths.

We have measured eight nominally identical nanowire arrays on the same sample, with their lasing spectra shown in Fig. 5 (b). Although no device showed lasing from all curved arrays, five common lasing wavelengths can be identified, suggesting that the lasing mechanism is that described by simulations. We assign the lasing lines at 1288 nm, 1297 nm, 1305 nm, 1324 nm and 1328 nm to arcs 2, 3, 4, 5 and 6 respectively. Arc 1 is unlikely to lase due to its very low Q factor. Some lasing lines appear outside of the five common wavelengths. These can be attributed to other resonant modes introduced by the nanowire nonuniformity.

There is a slight discrepancy between the measured and simulated lasing wavelengths which can be attributed to experimental factors such as the change in local effective refractive index due to nonuniformity in nanowire size or in the InGaAs composition, and to simulation related factors such as imperfect meshing. The jump in wavelength from the first four arcs to the last two can be explained by the nanowire diameter being slightly larger on the outside of the array. This is due to the larger diffusion area available for the nanowires to draw precursors from.

The previous simulations have shown arc 1 to be very lossy due to its short cavity length. For the other arcs, a major factor that can impede lasing is the nonuniformity in the nanowire size which leads to a decrease of Q factor and increase of the lasing threshold. It's possible that the pumping power was not high enough to cause lasing in the less uniform arcs. Moreover, the position of the outlier nanowire is important, as the impact of the NW on the mode increases with mode overlap. A single nonuniform nanowire in the center of the array will cause much more scattering than one placed at the ends.

We continue by analyzing the lasing properties of one representative array in more detail. The measured emission spectrum from the full nanowire array structure is shown in Fig. 6(a). At low

pumping powers, the lasing spectrum is single mode around 1305 nm. At increased pumping power, multiple lasing modes emerge at different lasing thresholds and slope efficiencies. This difference is likely due to the difference in their Q factors caused by the nonuniform nanowire diameters. The nanowires show a reasonably uniform gain spectrum around 1300-1330 nm, which is unlikely to have a noticeable effect on the lasing threshold. The gain spectrum is broadened by InGaAs compositional changes at the edges of the nanowire [28].

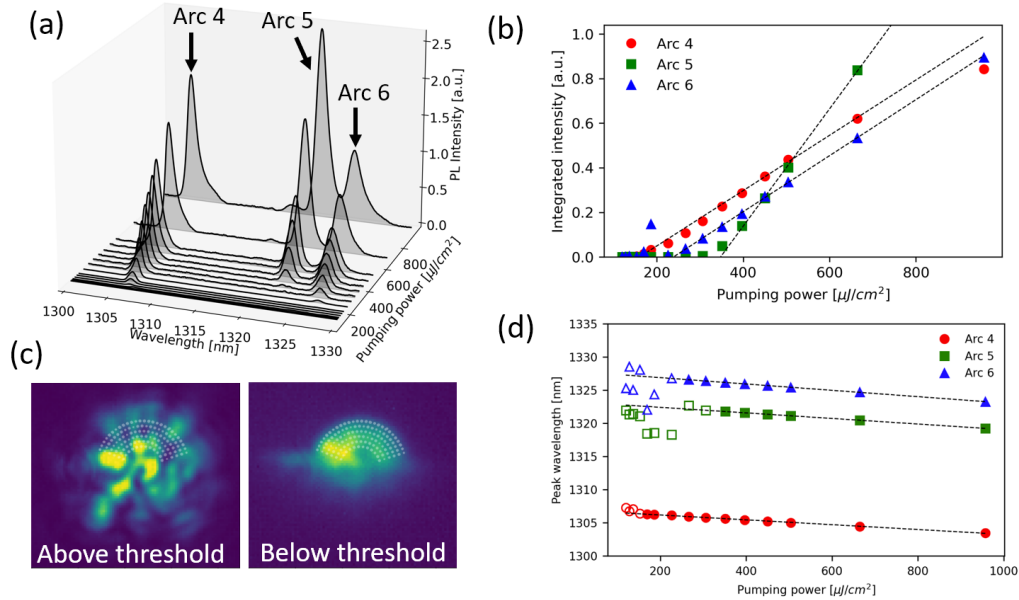


Fig. 6. Optical characterization of a representative nanowire array structure. (a) Power dependent PL emission showing the evolution of the lasing spectrum. (b) L-L curves of the three lasing peaks along with linear fits in the above threshold regions. (c) Near field emission of the array before and after the lasing threshold, showing characteristic interference patterns, along with a transparent SEM overlay of the array structure. (d) Peak wavelength as a function of pumping power along with fits in the above threshold region. The hollow markers represent data points below the threshold.

The L-L curves of the three lasing peaks are shown in Fig. 6(b). A threshold power density of $157 \mu\text{J}/\text{cm}^2$ is extracted for arc 4. Arcs 5 and 6 show thresholds of 347 and $238 \mu\text{J}/\text{cm}^2$ respectively. These values are in line with other thresholds of III-V nanowire photonic crystal lasers at room temperature [16,19,26,20]. The Q factor can be approximated using the full width at half maximum of the lasing peaks immediately after the threshold. This method overestimates the Q factor, however the comparison between different arc is still meaningful. From the measurement, arcs 4, 5 and 6 have Q factors of 2311, 1114 and 1407 respectively. The Q factor is well correlated with the lasing threshold for each arc, showing the importance of nanowire uniformity.

Figure 6(c) shows the near field emission images captured by the InGaAs focal plane array detector at below and above lasing thresholds. We observe that the speckle pattern is oriented towards the back of the array, indicating that light is preferentially emitted towards the back of the array. This agrees with the results of the simulations presented in Fig. 3. The lasers show good wavelength stability with no mode hopping at increased pumping powers as seen in Fig. 6(d). The slight redshift can be attributed to the self-heating of the laser causing a change in the effective refractive index of the cavity. Both the refractive index of the nanowire, and

the nanowire diameter increase with temperature, leading to an increase in wavelength. The refractive index dependence on temperature is two orders of magnitude higher than the thermal expansion index, indicating that refractive index change is the main redshift mechanism.

5. Conclusion

In conclusion, we have presented both simulation and experimental studies of curved nanowire array lasers made of InGaAs nanowires directly grown on silicon-on-insulator substrates. The FDTD simulations show minimal change of the Q factor due to cavity bending, which paves the way for arbitrary cavity shapes with high Q factors. The properties of the emitted beam were simulated, showing an interference pattern in the far field due to the high divergence. With the curved cavity, we have demonstrated room-temperature lasing at telecom O-band wavelengths with a laser threshold of $157\mu\text{J}/\text{cm}^2$. For future development of such lasers, improvements in the epitaxy procedure are needed to increase nanowire uniformity. These results thus highlight the potential of using nanowires for ultra-compact photonic crystal lasers with novel geometries.

Funding. Engineering and Physical Sciences Research Council funded Future Compound Semiconductor Manufacturing Hub (EP/P006973/1); European Regional Development Fund (80762-CU145 (East)).

Acknowledgments. This work was partially supported by the European Regional Development Fund through the Welsh Government (80762-CU145 (East)); and the Future Compound Semiconductor Manufacturing Hub [grant number EP/P006973/1].

Disclosures. The authors declare no conflicts of interest.

Data availability. The data that support the findings of this study are available via the Cardiff University Research Portal [29].

References

1. S. Noda, K. Kitamura, T. Okino, D. Yasuda, and Y. Tanaka, "Photonic-Crystal Surface-Emitting Lasers: Review and Introduction of Modulated-Photonic Crystals," *IEEE J. Sel. Top. Quantum Electron.* **23**(6), 1–7 (2017).
2. M. A. Butt, S. N. Khonina, and N. L. Kazanskiy, "Recent advances in photonic crystal optical devices: A review," *Opt. Laser Technol.* **142**, 107265 (2021).
3. Y.-H. Hong, W.-C. Miao, W.-C. Hsu, K.-B. Hong, C.-L. Lin, C. Lin, S.-C. Chen, and H.-C. Kuo, "Progress of Photonic-Crystal Surface-Emitting Lasers: A Paradigm Shift in LiDAR Application," *Crystals* **12**(6), 800 (2022).
4. W. Zheng, "Semiconductor photonic crystal laser," *Chin. Phys. B* **27**(11), 114211 (2018).
5. S. Matsuo, T. Sato, K. Takeda, A. Shinya, K. Nozaki, E. Kuramochi, H. Taniyama, M. Notomi, T. Fujii, and K. Hasebe, "Photonic crystal lasers using wavelength-scale embedded active region," *J. Phys. D: Appl. Phys.* **47**(2), 023001 (2014).
6. M. Saldutti, M. Xiong, E. Dimopoulos, Y. Yu, M. Gioannini, and J. Mørk, "Modal Properties of Photonic Crystal Cavities and Applications to Lasers," *Nanomaterials* **11**(11), 3030 (2021).
7. D. Miller, "Device requirements for optical interconnects to silicon chips," *Proc. IEEE* **97**(7), 1166–1185 (2009).
8. K. Tanabe, M. Nomura, D. Guimard, S. Iwamoto, and Y. Arakawa, "Room temperature continuous wave operation of InAs/GaAs quantum dot photonic crystal nanocavity laser on silicon substrate," *Opt. Express* **17**(9), 7036–7042 (2009).
9. K. Takeda, T. Sato, T. Fujii, E. Kuramochi, M. Notomi, K. Hasebe, T. Kakitsuka, and S. Matsuo, "Heterogeneously integrated photonic-crystal lasers on silicon for on/off chip optical interconnects," *Opt. Express* **23**(2), 702–708 (2015).
10. K. Takeda, T. Tsurugaya, T. Fujii, A. Shinya, Y. Maeda, T. Tsuchizawa, H. Nishi, M. Notomi, T. Kakitsuka, and S. Matsuo, "Optical links on silicon photonic chips using ultralow-power consumption photonic-crystal lasers," *Opt. Express* **29**(16), 26082–26092 (2021).
11. G. Crosnier, D. Sanchez, S. Bouchoule, P. Monnier, G. Beaudoin, I. Sagnes, R. Raj, and F. Raineri, "Hybrid indium phosphide-on-silicon nanolaser diode," *Nat. Photonics* **11**(5), 297–300 (2017).
12. T. Jung, R. Herrick, J. Norman, K. Turnlund, C. Jan, K. Feng, A. C. Gossard, and J. E. Bowers, "Impact of threading dislocation density on the lifetime of InAs quantum dot lasers on Si," *Appl. Phys. Lett.* **112**(15), 153507 (2018).
13. T. Zhou, M. Tang, G. Xiang, B. Xiang, S. Hark, M. Martin, T. Baron, S. Pan, J. S. Park, Z. Liu, and S. Chen, "Continuous-wave quantum dot photonic crystal lasers grown on on-axis Si (001)," *Nat. Commun.* **11**(1), 977 (2020).
14. K. Tomioka, Y. Kobayashi, J. Motohisa, S. Hara, and T. Fukui, "Selective-area growth of vertically aligned GaAs and GaAs/AlGaAs core-shell nanowires on Si(111) substrate," *Nanotechnology* **20**(14), 145302 (2009).
15. K. Tomioka and T. Fukui, "Recent progress in integration of III–V nanowire transistors on Si substrate by selective-area growth," *J. Phys. D: Appl. Phys.* **47**(39), 394001 (2014).

16. W. Lee, H. Kim, J. You, and D. L. Huffaker, "Ultracompact bottom-up photonic crystal lasers on silicon-on-insulator," *Sci. Rep.* **7**(1), 9543 (2017).
17. H. Kim, W. J. Lee, A. C. Farrell, A. Balgarkashi, and D. L. Huffaker, "Telecom-wavelength bottom-up nanobeam lasers on silicon-on-insulator," *Nano Lett.* **17**(9), 5244–5250 (2017).
18. T. Chang, H. Kim, B. T. Zutter, W. Lee, B. C. Regan, and D. L. Huffaker, "Orientation-controlled selective-area epitaxy of III-V nanowires on (001) silicon for silicon photonics," *Adv. Funct. Mater.* **30**(30), 2002220 (2020).
19. H. Kim, W. J. Lee, A. C. Farrell, J. S. D. Morales, P. Senanayake, S. V. Prikhodko, T. J. Ochalski, and D. L. Huffaker, "Monolithic InGaAs nanowire array lasers on silicon-on-insulator operating at room temperature," *Nano Lett.* **17**(6), 3465–3470 (2017).
20. A. C. Scofield, S.-H. Kim, J. N. Shapiro, A. Lin, B. Liang, A. Scherer, and D. L. Huffaker, "Bottom-up Photonic Crystal Lasers," *Nano Lett.* **11**(12), 5387–5390 (2011).
21. D. Goldring, U. Levy, and D. Mendlovic, "Highly dispersive micro-ring resonator based on one dimensional photonic crystal waveguide design and analysis," *Opt. Express* **15**(6), 3156–3168 (2007).
22. Y. Zhang, C. Hamsen, J. T. Choy, Y. Huang, J.-H. Ryou, R. D. Dupuis, and M. Loncar, "Photonic crystal disk lasers," *Opt. Lett.* **36**(14), 2704–2706 (2011).
23. T. W. Lu, W. C. Tsai, T. Y. Wu, and P. T. Lee, "Laser emissions from one-dimensional photonic crystal rings on silicon-dioxide," *Appl. Phys. Lett.* **102**(5), 051103 (2013).
24. G. Gao, Y. Zhang, H. Zhang, Y. Wang, Q. Huang, and J. Xia, "Air-mode photonic crystal ring resonator on silicon-on-insulator," *Sci. Rep.* **6**(1), 19999 (2016).
25. H.-T. Lin, K.-S. Hsu, C.-C. Chang, W.-H. Lin, S.-Y. Lin, S.-W. Chang, Y.-C. Chang, and M.-H. Shih, "Photonic Crystal Circular Nanobeam Cavity Laser with Type-II GaSb/GaAs Quantum Rings as Gain Material," *Sci. Rep.* **10**(1), 4757 (2020).
26. C. Messina, Y. Gong, O. Abouzaid, B.-P. Ratiu, T. Grieb, Z. Yan, A. Rosenauer, S. S. Oh, and Q. Li, "Deformed honeycomb lattices of InGaAs nanowires grown on silicon-on-insulator for photonic crystal surface emitting lasers," *Adv. Opt. Mater.* **11**(5), 2201809 (2023).
27. D. Greace and L. C. Andreani, "Effects of disorder on propagation losses and cavity Q-factors in photonic crystal slabs," *Photonics Nanostruct.* **3**(2-3), 120–128 (2005).
28. D. Rudolph, S. Funk, M. Döblinger, S. Morkötter, S. Hertenberger, L. Schweickert, J. Becker, S. Matich, M. Bichler, D. Spirkoska, I. Zardo, J. J. Finley, G. Abstreiter, and G. Koblmüller, "Spontaneous Alloy Composition Ordering in GaAs-AlGaAs Core-Shell Nanowires," *Nano Lett.* **13**(4), 1522–1527 (2013).
29. Cardiff University, "Data for curved InGaAs nanowire array lasers grown directly on silicon-on-insulator," Cardiff University Research Portal 2023, <http://doi.org/10.17035/d.2023.0279873657>.